



This is a repository copy of *On deformation characterisation of machined surfaces and machining-induced white layers in a milled titanium alloy*.

White Rose Research Online URL for this paper:
<https://eprints.whiterose.ac.uk/178294/>

Version: Published Version

Article:

Brown, M. orcid.org/0000-0002-0937-9139, M'saoubi, R., Crawforth, P. orcid.org/0000-0002-1235-8494 et al. (3 more authors) (2022) On deformation characterisation of machined surfaces and machining-induced white layers in a milled titanium alloy. *Journal of Materials Processing Technology*, 299. 117378. ISSN 0924-0136

<https://doi.org/10.1016/j.jmatprotec.2021.117378>

Reuse

This article is distributed under the terms of the Creative Commons Attribution (CC BY) licence. This licence allows you to distribute, remix, tweak, and build upon the work, even commercially, as long as you credit the authors for the original work. More information and the full terms of the licence here:
<https://creativecommons.org/licenses/>

Takedown

If you consider content in White Rose Research Online to be in breach of UK law, please notify us by emailing eprints@whiterose.ac.uk including the URL of the record and the reason for the withdrawal request.



eprints@whiterose.ac.uk
<https://eprints.whiterose.ac.uk/>



On deformation characterisation of machined surfaces and machining-induced white layers in a milled titanium alloy

M. Brown^{a,e}, R. M'Saoubi^b, P. Crawforth^c, A. Mantle^d, J. McGourlay^d, H. Ghadbeigi^{e,*}

^a Industrial Doctoral Centre in Machining Science, Advanced Manufacturing Research Centre with Boeing, University of Sheffield, Rotherham, S60 5TZ, UK

^b R&D Materials & Technology Development, Seco Tools AB, SE73782, Fagersta, Sweden

^c Advanced Manufacturing Research Centre with Boeing, University of Sheffield, Rotherham, S60 5TZ, UK

^d Rolls-Royce PLC, Derby, UK

^e The University of Sheffield, Department of Mechanical Engineering, Sir Frederick Mappin Building, Mappin Street, S1 3JD, Sheffield, UK

ARTICLE INFO

Associate Editor: Erhan Budak

Keywords:

White layer
Swept grain
Micro-grid
Machining
Plastic strain

ABSTRACT

Machining-induced white layers and severely deformed layers are undesirable surface integrity features which can be formed when machining high-strength aerospace alloys. An orthogonal milling process has been designed and performed to assess the impact of cutting speeds, tool wear, cutting edge radius and climb vs conventional milling on white layer formation and plastic strain distribution. The plastic deformation in the machined surface associated with the formation of white layers in Ti-6Al-4V has been quantified using micro-grids of different length scales printed using the electron beam lithography technique. It was found that white layers formed via the severe plastic deformation mechanism, at equivalent plastic strain values in excess of 1.2 and in regions of the cutting arc with the instantaneous chip thickness of less than the cutting-edge radius and ploughing and rubbing being the dominant mechanisms. The results indicated that the magnitude of the measured strains and the depth of plastically deformed material was greater at lower cutting speeds, during climb milling and when machining with a larger cutting edge radius and tool flank wear land.

1. Introduction

Machining-induced white layers can be formed when a difficult-to-cut material, such as aerospace superalloys or hardened steels, is machined at high cutting speeds (Chou and Evans, 1999) or using a severely worn tools (Brown et al., 2019) or alternatively tools with a large radius of curvature (Denkena et al., 2015). Griffiths (1987), identified that these white layers can form via a thermally driven phase transformation mechanism or a severe plastic deformation (SPD) mechanism due to mechanical work, which can involve dynamic recrystallisation. Irrespective of the material among the common aerospace engine alloys, the white layer region typically possesses a highly refined nanoscale grain structure, increased hardness relative to the bulk material and extreme residual stresses, as shown by Brown et al. (2018) for Ti-6Al-4V, Bushlya et al. in IN-718 (Bushlya et al., 2011) and hardened steel (Fang-yuan et al., 2017). Whilst these properties may appear beneficial in certain circumstances, Herbert et al. (2014) have shown that the presence of a white layer can lead to a significant reduction in the fatigue life of components, compared to surfaces without a white

layer but similar levels of residual stress. As such, the presence of a white layer or very severely deformed layer in an aeroengine component is not tolerated. The phase transformation mechanism is associated with the high cutting speeds, whilst the SPD mechanism can dominate at lower speeds, as identified by Hosseini et al. (2015). Guo et al. (2010) reported that, due to the greater heat generation at higher speeds, phase transformation white layers can be associated with a more tensile residual stress state, relative to an SPD white layer in the same material.

Traditionally, destructive cross-sectional microscopy is required to detect a white layer, although recent work, such as that by Brown et al. (2021) has shown that x-ray diffraction peak broadening measurements facilitate white layer detection in a range of aerospace alloys. However, this is an emerging technique in this application and due to the current reliance on destructive testing for white layer detection in industry, it is appropriate to investigate the fundamental theory behind white layer formation to help prevent its occurrence. It is therefore critical to characterise the mechanical work threshold for SPD white layers, which can be determined through quantification of plastic deformation.

In addition to white layers, the severely deformed material at the

* Corresponding author.

E-mail address: h.ghadbeigi@sheffield.ac.uk (H. Ghadbeigi).

<https://doi.org/10.1016/j.jmatprotec.2021.117378>

Received 22 April 2021; Received in revised form 10 September 2021; Accepted 15 September 2021

Available online 20 September 2021

0924-0136/© 2021 The Author(s). Published by Elsevier B.V. This is an open access article under the CC BY license (<http://creativecommons.org/licenses/by/4.0/>).

machined surface, i.e., the swept grain region, plays a critical role in the functional performance of machined parts where no white layers are formed, as reported by Hardy et al. (2014). Swept grain (also called distorted layer or surface drag) is the plastic deformation of the material in the near surface of a workpiece in the direction of the cutting velocity (Edkins et al., 2014). Swept grain thickness can vary from layers thinner than 3 μm (Edkins et al., 2014) up to layers over 250 μm thick (Zhou et al., 2011). Whilst Elmadagli and Alpas (2003) have shown that the angle of grain distortion can be used to estimate the imposed plastic deformation within the swept grain region, due to ultra-fine grain size in the white layer region, it is not possible to measure this plastic strain from optical micrographs of the etched cross-section. As such, alternative methods are required to measure strain throughout the machined sub surface.

Attempts have already been made to measure the plastic deformation during machining. Early work by Childs (1971) measured flow patterns during orthogonal cutting using grids with a 25 μm pitch (the distance between the grind lines) and a 5 μm line width, however, these grids were inscribed into the surface and therefore may have influenced subsequent deformation due to changes in local stress concentration near the grids. Ghadbeigi et al. (2008) used electron beam lithography (EBL) to produce microgrids with 10 μm pitch and a 1 μm line width to measure the strain imparted in the machined surface during low-speed orthogonal cutting of an aluminium alloy. Although a very low cutting speed (2.4 m/min) was used in the experiment, they showed that the applied method enables measurement of the strain even in regions of large strain gradient in the grids adjacent to the machined surface. In a recent study Sela et al. (2020) used microgrids with a pitch of 40 μm generated by micro-milling to quantify the surface drag in machined Ti-6Al-4V. The authors measured that the depth of the plastically deformed layer according to the deformed grids exceeded that value obtained during conventional optical microscopy surface integrity inspection.

When investigating white layer formation in nickel superalloys, Ranganath et al. (2009), implemented finite element modelling to predict materials deformation at the onset of white layer formation in nickel superalloys and reported a strain of up to 1.2 in the swept grain material, with greater strain at lower speeds and larger cutting edge radii. Nie et al. (2020) reported the only results for experimental strain measurement within the white layer, the authors used micro-grids of 10 μm pitch were produced by Focused Ion Beam (FIB) etching. A plastic strain threshold of 0.65 was measured for white layer formation in the AISI52100 material under investigation. Both dry and cryogenic cooling were used with mechanical effects more dominant when using cryogenics, however it is not apparent whether the white layer formed under dry conditions was primarily due to the phase transformation mechanism. Given that the thickest reported white layer was about 1.82 μm thick, a higher resolution deformation measurement, i.e. grids smaller than 2 μm would be required, to quantify strain within the white layer. Additionally, the etched grooves could adversely affect the stress concentration and deformation mechanics in regions adjacent to the grid grooves, due to the severity of deformation during white layer formation. With respect to nickel superalloys, modelling methods are mostly used to quantify materials deformation at the onset of white layer formation. To the best knowledge of the authors, there has been no quantitative experimental or theoretical investigation into the plastic strains associated with white layer formation in a titanium alloy.

In the studies highlighted above, finite strain plasticity principles are implemented in non-contact full-field and local deformation characterisation techniques such as digital image correlation (DIC) and micro-grid techniques. In both techniques local strain distributions are determined from local displacement fields. In the DIC technique, the plastic deformation is measured by monitoring the evolution of the displacement field which is made visible by tracking a speckle pattern on the surface (Pottier et al., 2014). By contrast in microgrid methods, the deformed grid patterns are then used to calculate the local plastic deformation

field relative to the undeformed grid pattern, as outlined by Allais et al. (1994). The microgrids can be produced by EBL or focused ion beam etching (Nie et al., 2020).

Although the DIC technique has been widely used in the structural integrity assessment of materials and structures, severe technical challenges are involved when it is applied in metal machining as only dry cutting can be implemented due to the necessity of continuous monitoring of the deformation field. Additionally, the method is less suited to strain measurement in the workpiece region immediately adjacent to the tool, i.e. at the machined surface, due to fuzzy delimitation of the cutting tool in the image, as identified by Pottier et al. (2014). On the other hand, the application of the micro-grid techniques resolves this challenge given that pre- and post-deformation grid configurations are needed, however they do not provide the deformation field evolution throughout the chip formation. In addition, the true plane strain deformation condition can easily be achieved using the microgrids technique when the out of plane deformation is confined by application of a supporting material as indicated by Ghadbeigi et al. (2008). Both DIC and micro-grid methods for strain measurement have been directly compared in an in-situ tensile test where scanning electron microscope (SEM) micrographs of deforming microstructure were used for DIC measurements while square grids of gold with 10 μm pitch were printed on the etched surface of a steel alloy prior to the testing for micro-grid measurements (Ghadbeigi et al., 2012). Reasonable agreement (16 % error) was found between both methods, with the micro-grid method being judged more appropriate for the quantitative measurement of plastic strain due to more direct characterisation and less random microscopy imaging artifacts involved that could affect the DIC algorithm predictions.

This paper will, therefore, investigate the level and depth of plastic strain experienced by the material at the machined surface during white layer formation in milling using microgrid methods, considering not only the white layer formation but also the swept grain region. Titanium will be used rather than the AISI52100 steel used in previous work in the literature as white layers form only through SPD, unless employing very high cutting speeds (Xu et al., 2019), whereas phase transformation white layers readily form on AISI52100 steel (Umbrello, 2013). The effect of cutting speed, insert wear and cutting edge radii on the tendency for SPD white layer formation during milling and the resulting plastic strain distributions are examined, as these machining conditions are widely reported to influence white layer formation irrespective of the workpiece material. Different milling strategies are also compared to quantify the effects of chip formation mechanics on the deformation evolution and white layer formation. The results are used to propose a critical threshold for SPD white layer generation in a titanium alloy.

2. Experimental methods

A custom rig, as shown in Fig. 1, was designed such that a Seco Tools R220.17-0040-16 tool holder, modified for single-point milling, and TPUN160308 HX uncoated carbide inserts could be used to orthogonally cut the mill-annealed Ti-6Al-4V workpieces clamped in the rig. The orthogonal milling setup simplifies the deformation mechanics during chip formation and ensures the material deforms in plane strain mode in

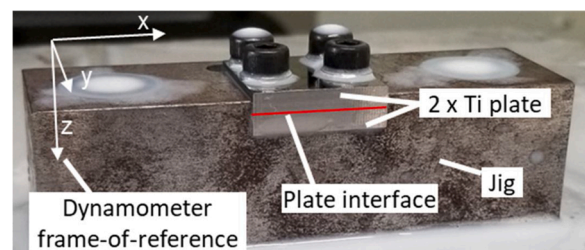


Fig. 1. The workpieces and jig mounted in the machining centre.

the midplane of the samples. Two workpiece samples with a size of $25.5 \times 24.5 \times 4$ mm were used in the rig, with one side of each sample polished before the experiments to achieve a mirror-finish required for printing the micro-grids. The samples were mounted such that the polished faces, with the printed micro-grids, were contacting and clamped tightly to satisfy plane strain deformation condition. The machining setup and the interaction of the tool with the workpiece for climb and conventional milling are illustrated in Fig. 2(a) and (b), respectively. To preserve the machined surface, the tool was rapidly disengaged in the y-direction at the end of cut.

2.1. Deformed surface generation

Orthogonal milling was carried out on Ti-6Al-4V to generate machined surfaces with and without white layers and different levels of deformation. The cutting experiments were performed on a DMG Mori NVX5080 machining centre using flood Blaser Vasco 7000 coolant with the cutting forces measured using a Kistler force dynamometer. Unworn and naturally worn cutting inserts as well as inserts with an artificial wear land of 0.5 mm produced for the trials on the clearance face were used to compare the effect of wear geometry on the machining-induced plastic deformation and surface integrity. This large wear land was selected based on previous work of Brown et al. (2019) that showed white layers as thick as $15 \mu\text{m}$ were generated at high wear levels. The new inserts had a rake angle of 0° in the radial and axial directions and a clearance angle of 11° when mounted in the tool holder. The artificially worn inserts were prepared at an angle of 12° from the clearance face, as shown in Fig. 3, such that the wear land would have a clearance of -1° , i.e. it would contact the surface. Additionally, the artificially worn inserts were prepared to have a cutting edge radius of $85 \mu\text{m}$ and $10 \mu\text{m}$, to investigate the resultant effect on the induced deformation. For each trial, the engagement of the cutting tool was adjusted to account for the material removed from the worn inserts and maintain a programmed 0.5 mm depth of cut. A feed of 0.5 mm/tooth was selected for the trials to analyse the contribution of size effect on the applied deformation and the white layer formation process as this ensures a large variation of the effective uncut chip thickness along the tool engagement arc compared to the associated cutting edge radii of the inserts.

Table 1 outlines the selected inserts used to generate surfaces and the cutting conditions for the trials are reported in Table 2. The selected cutting speeds were adopted based on previous work of the authors (Brown et al., 2019) with increased thermal effects observed at the higher cutting speed of 80 m/min. Both climb and conventional milling operations were used to compare the effects of chip thickness evolution, thick-to-thin and thin-to-thick chip formation, respectively, on the white layer formation and the machining induced workpiece deformation. The trials listed in Table 2 are the surfaces for which strain maps are

presented in this paper, the full set of trials were a full factorial design with repeats. This subset of surfaces was down-selected to compare surfaces where only one independent variable had changed to isolate their effects.

2.2. Micro-grid preparation

The EBL technique, as described by Ghadbeigi et al. (2012), was used to print gold micro-grids with a thickness of 90 nm on a mirror-polished surface of the workpieces at the vicinity of the surface to be machined. A 10 nm layer of titanium between the gold layer and the workpiece was used to promote the adhesion of the grids. Each workpiece pair in the jig consisted of a micro-grid sample and a second polished sample, face-to-face, to ensure the two-dimensional plane strain deformation condition is achieved. Gold was used for the micro-grids due to its high melting point of 1064°C (ASM-International, 1990) and its large atomic number, which gives rise to a strong contrast on a back-scattered electron SEM image for deformation characterisation.

Four different micro-grid pitches, 5, 10, 20 and $40 \mu\text{m}$, as shown in Fig. 4(a), were used to ensure deformation could be captured at different length scales, considering the comparatively thin white layer thickness compared with the overall depth of deformation. Previous investigations revealed that grids smaller than $5 \mu\text{m}$ deform very severely under the applied machining conditions, as such, it would be very difficult to resolve the deformed configuration of the grids in subsequent SEM analysis. Therefore, the $5 \mu\text{m}$ grids were used as the upper bound for the deformation characterisation resolution and it was expected to provide the required resolution to measure strain within the white layer. The grid line thicknesses were 10 % of the pitch and given that the grids are bonded to the surface rather than carved into them, the true deformation of the material will be presented by the deformed grids structures without altering the deformation mechanism. The grids were arranged as shown in Fig. 4(b) with the final machined surface passing through the grids as indicated in Fig. 4(c). The machined surface could then be examined using any of the four different grid resolutions. The resultant cutting arc on the machined surface can be separated into the region of cutting with chip formation during the final pass and a region of rubbing without chip formation as shown in Fig. 5.

It should be noted that the grid samples were used as the top or bottom sample when clamped against the polished sample in the jig, to ensure that all grid resolutions were captured for both climb and conventional milling in the chip formation and rubbing regions of the cutting arc. The grid region selected for analysis was typically chosen based on the depth to which strain was measured and the desire to maximise resolution, however, due to severe distortion of the smaller grid sizes and damage such as grid delamination or smearing, the grid regions available were restricted in some cases. When directly comparing two

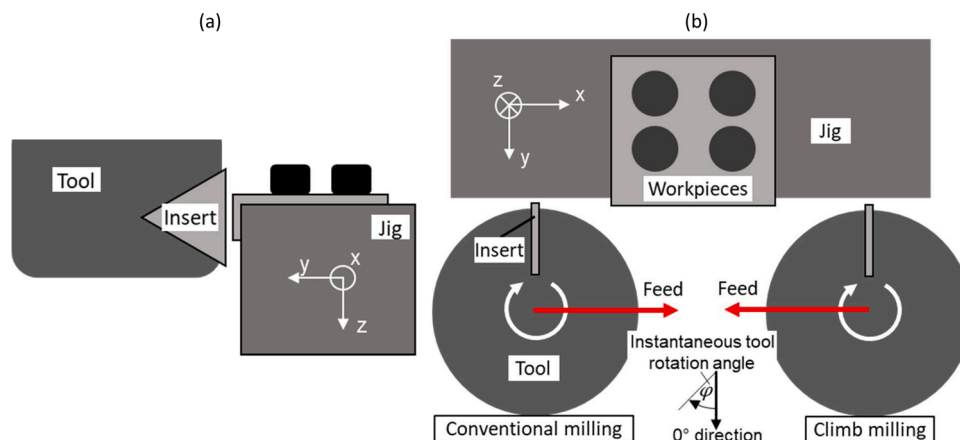


Fig. 2. Schematics of the cutting operation in (a) the y-z plane and (b) the x-y plane showing the interaction of the cutting insert with the workpiece material.

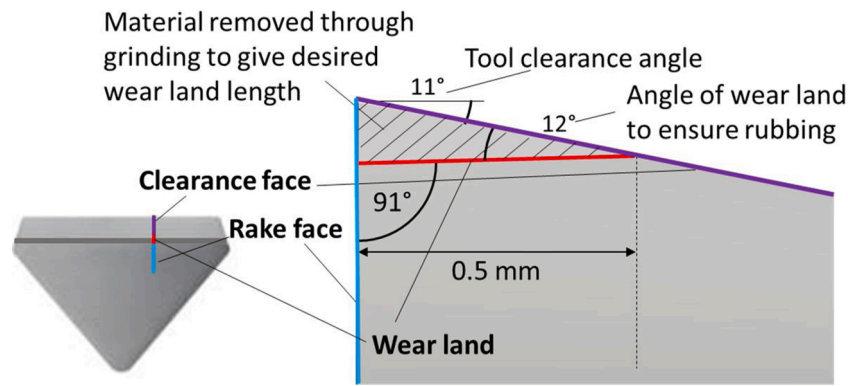


Fig. 3. A schematic highlighting the rake and clearance faces of the insert and the material removed to generate the artificial wear land.

Table 1
The cutting inserts used during the orthogonal milling trials to generate surfaces with different surface integrity states.

Insert type	Wear land (mm)	Cutting edge-radius (μm)
Unworn	0	30
Artificially worn	0.5	11–13
Artificially worn and re-honed	0.5	85–95
Naturally worn	0.265	137

surfaces, it was important to assess the same region of the cutting arc and therefore have the same grid resolution.

2.3. Strain measurement

Following machining, the strain in the orthogonally milled surfaces was calculated using the method outlined by Allais et al. (1994) by comparing SEM images of deformed and undeformed grids. An image processing interface was designed in MATLAB (Withers and Bhadeshia, 2001) and utilised to extract the coordinates of grid intersections from the SEM images of the deformed and undeformed grids. The intersections were then passed through a series of scripts to calculate the strain in the material according to the finite plastic deformation theory, as reported by Lee (1969) and presented as a surface plot. This is

Table 2
Selected cutting conditions from the Ti-6Al-4 V orthogonal milling trials. The cutting speed, insert wear, edge radius and milling tool rotation were varied to produce surfaces with differing levels of imparted strain.

Experiment No.	Cutting Speed V_c (m/min)	Insert wear VB (mm)	Cutting edge radius (μm)	Axial DoC a_p (mm)	Radial DoC a_e (mm)	Feed per tooth f_t (mm/tooth)	Climb/conventional milling
I	20	0.265	137	8	0.5	0.5	Conventional
II	20	0	30	8	0.5	0.5	Climb
III	20	0.5	86	8	0.5	0.5	Climb
IV	80	0.5	13	8	0.5	0.5	Conventional
V	80	0.5	86	8	0.5	0.5	Climb
VI	80	0.5	93	8	0.5	0.5	Conventional

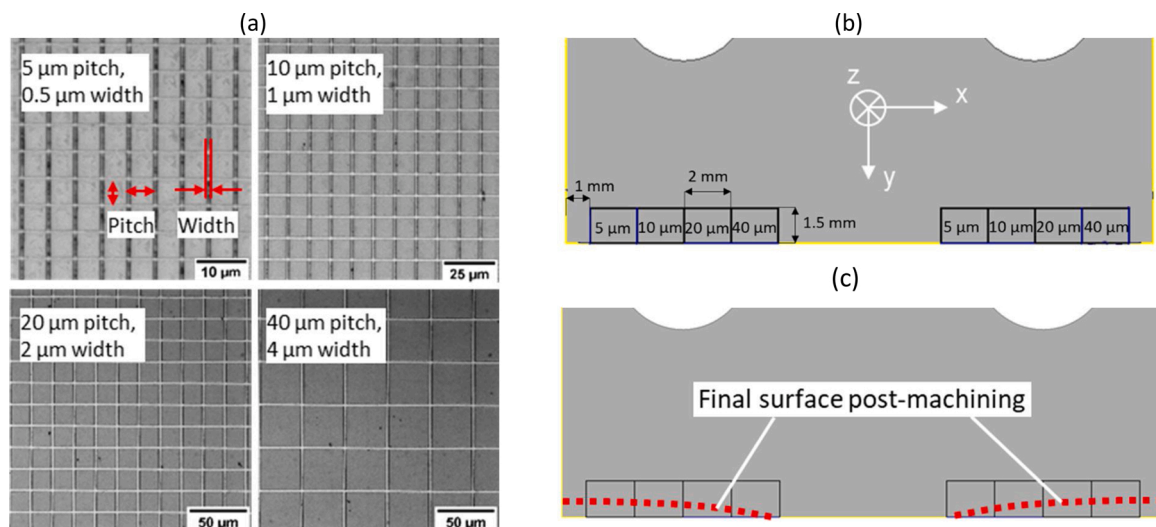


Fig. 4. (a) SEM micrographs of the undeformed micro-grids developed by the EBL technique with various grids pitch and grid line width with (b) the location of the grids along the cutting edge of the sample and (c) the final surface post-machining.

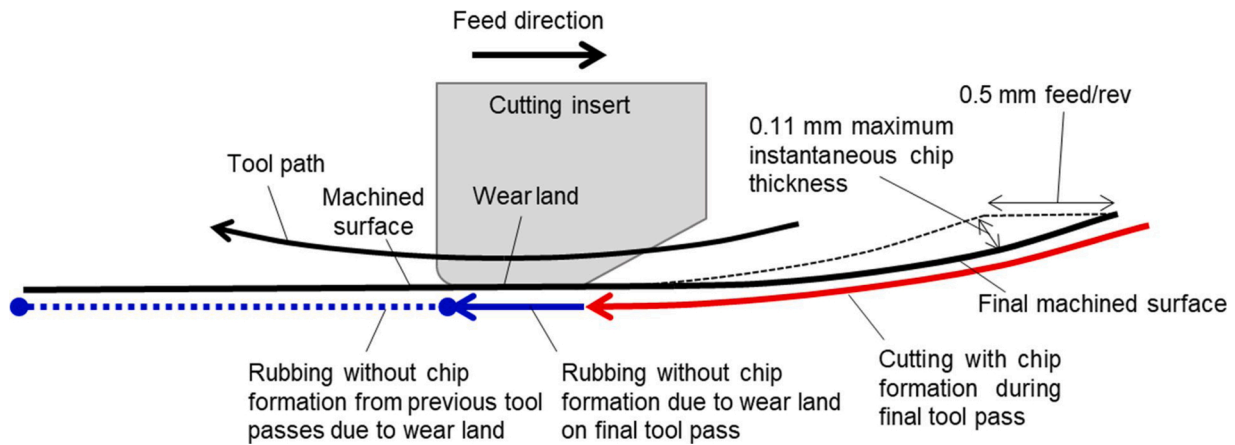


Fig. 5. A schematic outlining the key regions of the machined surface, the final cutting arc is made up of the final tool pass, plus the region with rubbing but no chip formation. Beyond the final cutting arc are the rubbing regions from previous insert passes. This diagram shows climb milling, the same regions are found for conventional milling with the tool path reversed.

outlined in the Appendix.

2.4. Microstructural assessment

Following the deformation characterisation, the specimens were prepared for optical microscopy by polishing with colloidal silica to remove the micro-grids and surface imperfections, such as scratches, without removing a significant amount of workpiece material. Additional grinding and polishing steps were not needed as the workpiece was already mirror-polished during the grid preparation steps. Kroll's reagent was used to etch the samples and reveal the grain structure. Microstructure image, of the same surface where the strain was measured were obtained with an Olympus BX51 microscope at 500x magnification or an Inspect F50 SEM for higher magnification images. EBSD was not undertaken as the texture pattern of the white layer was not of interest in this study and to prepare the sample to the very high surface quality require for EBSD may have required the removal of excess material, moving the microstructure assessment region away from the region where grid deformation was measured. Standard surface integrity assessment according to industry standards was conducted to determine the presence of any white layer. A surface integrity inspection failure due to the presence of a white layer is indicated by a tick or a cross on corresponding micrographs of a surface.

3. Results

The effect of tool condition and machining parameters on the formation of white layers and the associated plastic strains were assessed using quantification of the strain from the micro-grids and subsequent optical microscopy of the same regions. In Section 3.1, results from trials II and III are compared to isolate the influence of wear and IV and V are compared to isolate edge radius influence. Both are compared to trial I which varies wear land and edge radius. In Section 3.2, the effect of speed is isolated by comparing trials V and VII and in Section 3.3, climb and conventional milling are compared through trials V and VI.

3.1. The tool wear and edge radius effects on machining-induced surface deformation

The effect of tool wear on the machining-induced subsurface deformation and microstructure alteration as well as measured cutting forces are shown in Fig. 6, for machining with an unworn and a 0.5 mm worn insert. The true shear strain distributions generated by the unworn and artificially worn inserts and calculated with a 40 μm grid size at the machined surface are shown in Fig. 6(a) and (b), respectively. The 40 μm

grid region was used to compare the surfaces due to the large depth of deformation and the severity of the deformation which led to grid damage in regions with the smaller grid size for the surface created with a worn insert. While the shear strain barely reaches 5% in a surface machined by the fresh cutting edge (Fig. 6(a)) the worn inserts result in a severely deformed layer with a plastic strain over 0.6 approximately 40 μm beneath the machined surface. The etched micrograph of the same surfaces revealed that a white layer with a thickness of about 2.2 μm was generated by the worn tool (Fig. 6(d)), while no white layer was observed in the surface cut by the new insert (Fig. 6(c)). This is due to the presence of mechanically induced white layer formed through dynamic recrystallisation due to excessive ploughing of the material given the larger wear land and edge radius in the worn tool as has already reported for white layer formation in a milled titanium alloy (Brown et al., 2019). When cutting with the worn insert, the depth of cut achieved was only 0.28 mm, due to tool deflection, by contrast, with the unworn insert, the full 0.5 mm of material was removed. This corresponds to a maximum uncut chip thickness to cutting edge radius (a/r) ratio of 0.72 and 3.67 for the worn and unworn insert, respectively. The tool deflection is likely due to the high normal forces experienced when machining with the worn inserts, as shown in Fig. 6(f). The effect of this deflection and the cutting forces on the white layer formation and sub-surface plastic deformation is explored further in the Discussion section.

The strain profiles of Fig. 6(e) shows that the depth of the plastically deformed layer using the worn and sharp inserts can reach up to 125 μm and 75 μm below the machined surface, respectively, both of which are beyond the resolution achievable by analysing the optical micrographs of the deformed microstructure due to difficulties distinguishing low levels of grain distortion from the randomness of grain structure. The strain evolution profile for the worn tool, the solid lines in Fig. 6(e), indicates that the shear strain (ϵ_{xy}), in the most dominant followed by ϵ_{xx} and ϵ_{yy} (the strain in the x-direction and y-direction, respectively). The high shear strain can be linked to the larger normal and tangential forces measured near the end of the tool rotation where the tool flank face is in contact with the workpiece surface, thereby leading to increased dragging of the surface. This is not the case, however, for the sharp cutting edge as shown by the broken lines where the main deformation mode is compression normal to the machined surface with minimal shear deformation measured at the machined surface. The dominant compression in the sharp cutting edge could be associated with the ploughing and the tertiary deformation zone where the material is pushed below the flank side of the tool.

The evolution of cutting forces (Fig. 6(f)) shows that there is no out-of-plane cutting force, as intended, and the normal force (measured in

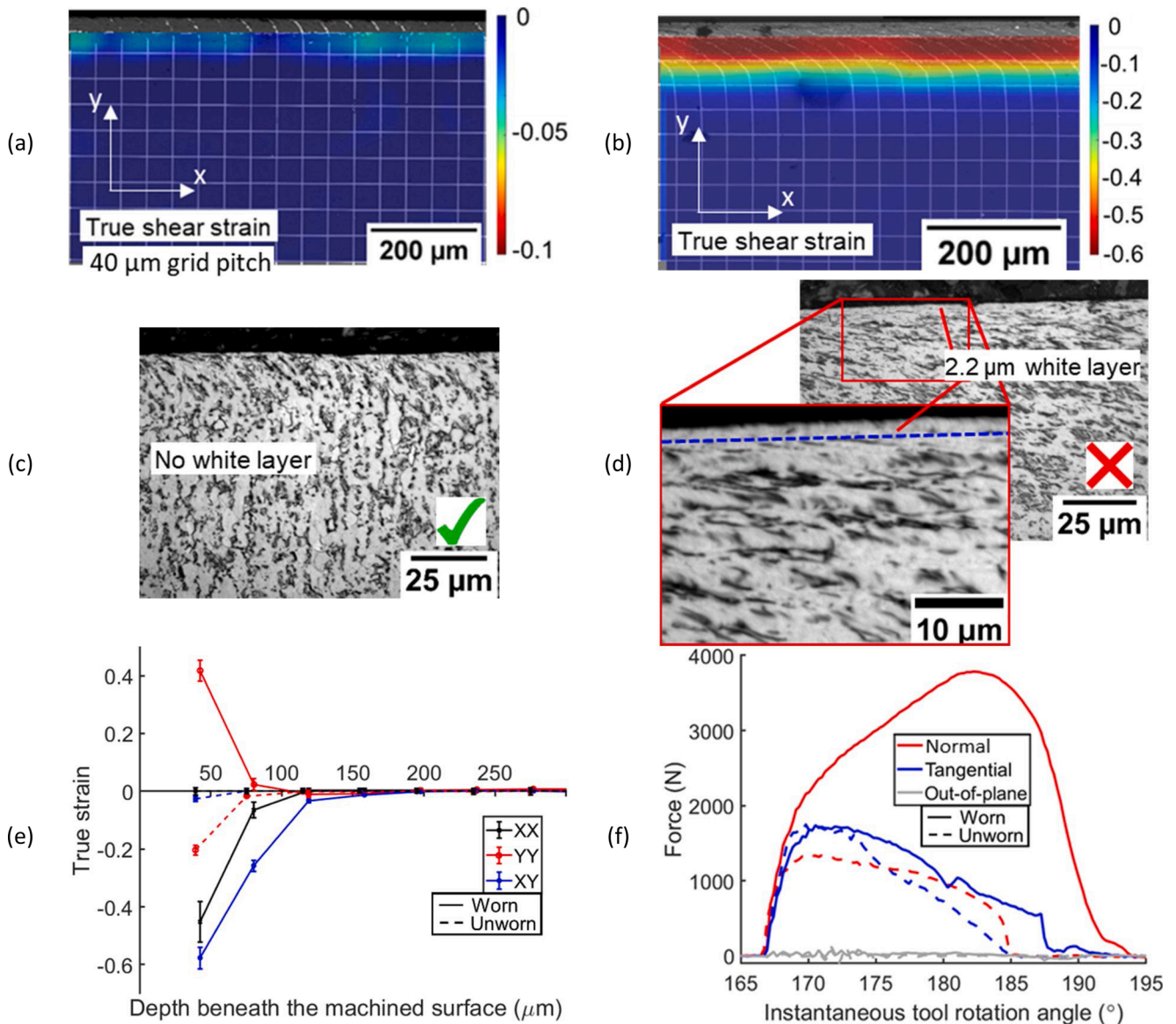


Fig. 6. True shear strain maps for a surface machined with (a) an artificially worn insert $VB = 0.5$ mm (trial III) and (b) an unworn insert (trial II) with corresponding optical micrographs in (c) and (d) respectively. The strain profiles and forces measured during machining are shown in (e) and (f). The tick and cross on the micrographs represent the pass/fail results of SI inspection. The grid pitch was $40 \mu\text{m}$.

the negative y-direction) is greatly affected by the tool wear. However, the normal force (solid red line) acts to compress the workpiece surface and yet the ϵ_{yy} profile (solid red line) indicates that the material is stretched in the near-surface region. This disparity arises due to the influence of deformation in the primary shear zone during chip formation and is explored further in the discussion section. The maximum forces for the new tool occur in the early stages of the tool rotation, which shows that material deforms and separates at the initial stages of contact, while for a worn tool, there is frictional contact of the relief side of the insert on the workpiece surface towards the end of the tool contact cycle for every tool rotation. This results in forces that continue to increase until the latter stages of the tool rotation when the tool is dragging across the surface.

Fig. 7(a) and (b) compares the effect of a small ($13 \mu\text{m}$) and large ($93 \mu\text{m}$) cutting-edge radii, respectively, on the developed deformation field in the workpiece, when the wear lands are identical. A grid size of $5 \mu\text{m}$ microns was implemented in this section of the cut, due to the vertical resolution required to capture the changes in the strain profiles with depth. The strain maps show that the larger cutting edge radius results in

a much deeper plastically deformed layer with shear strain 1.5 times larger than that observed in a surface machined with the smaller edge radius insert under identical cutting parameters. It should be noted that due to the excessive distortion of the grids when machining with a large edge radius insert, it was not possible to resolve the strain values at the machined surface itself. Strain could only be quantified at a depth greater than $8 \mu\text{m}$ where the maximum induced plastic strain is greater than 0.4 and could be more than 0.5 for the surface generated by the larger edge radius.

The optical micrographs in Fig. 7(c) and (d) show no evidence of a white layer on either surface, however, the surface machined with a large cutting edge radius possesses high levels of sub-surface deformation which gives rise to a large depth of swept grain (distorted) material. Although the depth of deformation is difficult to quantify from the optical micrograph, the measured strain profiles in Fig. 7(e) indicates that the material is plastically deformed beyond $50 \mu\text{m}$ below the produced surface. It should be noted that deformation normal to the machined surface is tensile for both edge conditions (ϵ_{yy} in Fig. 7(e)) immediately beneath the surface and decays to zero for the larger edge radius while

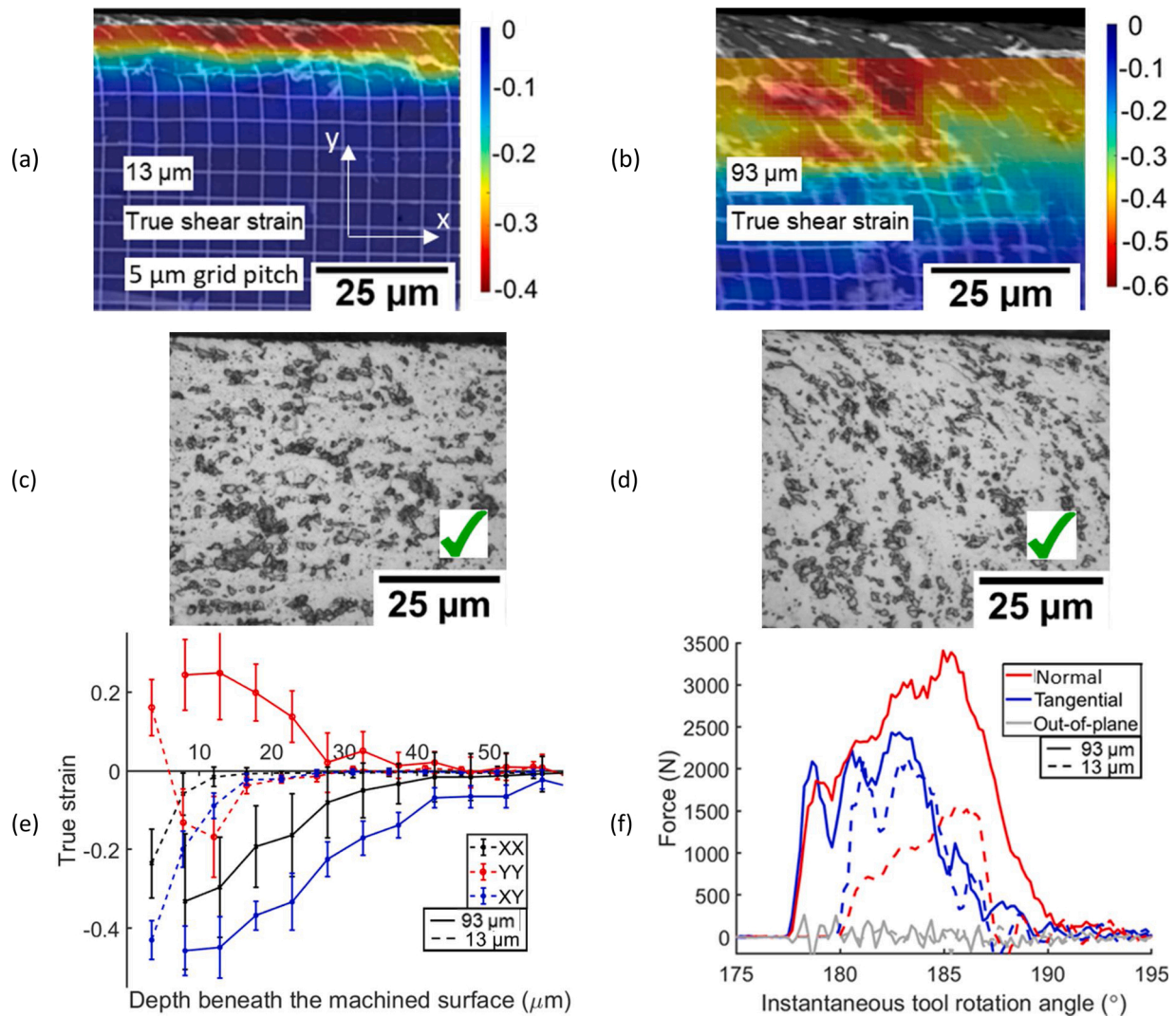


Fig. 7. True shear strain maps for a surface machined with an insert with (a) a 13 μm cutting edge radius (trial IV) and (b) a 93 μm cutting edge radius (trial VI) with corresponding micrographs in (c) and (d) respectively. The measured strain profiles and machining forces are shown in (e) and (f). The grid pitch was 5 μm .

ϵ_{yy} becomes compressive at approximately 7 μm beneath the surface when using the tool with a smaller edge radius. Although the strains in the X and Y directions are meant to show similar, but opposite, trends, due to volume conservation, this is not observed in the graphs associated with the surface milled with a tool having a cutting edge radius of 13 μm . Such a discrepancy can be linked to a possible out of plane deformation at the 2nd row of the grids in Fig. 7(a) leading to unrealistic compressive strains in the Y direction. The increased deformation with the large edge radius insert can be attributed to the normal force during machining which was 2–3 times greater than for a tool with a smaller cutting edge radius, as shown by the force plots in Fig. 7(f). The tangential force, by contrast, was comparable for both types of inserts which, consequently, indicates the normal cutting force has a significant influence on the level of plastic deformation imparted into the machined surface. In the trial with the larger edge radius, only a 0.37 mm depth of cut was achieved, whereas for the smaller edge radius managed to remove the desired 0.5 mm depth of cut. The corresponding maximum a/r , due to the reduced depth of cut with the large edge radius inserts was 0.88, whereas for the smaller edge radius insert it was 8.46. Therefore, as it was also shown in Fig. 6, the depth of cut achieved appears to also influence the level of the imparted deformation.

The evolution of cutting forces with the tool rotation (Fig. 7(f)) shows the larger edge radius insert results in a longer contact between

the workpiece and the cutting edge with the maximum normal force measured towards the end of engagement for both the cases where the chip is at its maximum thickness.

The largest subsurface deformation across all the trials was measured when machining with a naturally worn insert, as shown in Fig. 8(a–c), and this is reflected in the thickest measured white layer with a maximum thickness of 3.7 μm , Fig. 8(d). This naturally worn insert has a smaller wear land but a larger edge radius compared to the artificially worn inserts. Therefore, the edge radius, which influences the size effect and the ploughing effect, plays a more critical role than the generated wear land on the machining induced subsurface deformation and structural integrity of the produced part. The achieved depth of cut was less than 0.1 mm when machining with the naturally worn insert due to a large tool deflection because of the produced cutting forces, this depth of cut corresponds to a maximum a/r of just 0.16. Although the 5 μm grid size in the strain maps in Fig. 8(a–c) offers the highest resolution of all the grids used in this study, the grids are severely distorted in the first 10 μm beneath the surface so the deformed grids could not be identified, preventing a deformation measurement in the white layer itself. However, the strain evolution profiles in Fig. 8(e) show that the plastic strains at the machined surface must exceed an equivalent strain 1.2 with a compression (ϵ_{yy}) and drag strain (ϵ_{xx}) of about 0.7, as this level of strain was present at 10 μm beneath the surface, where a smaller deformation is expected. Despite a relatively uniform distribution of

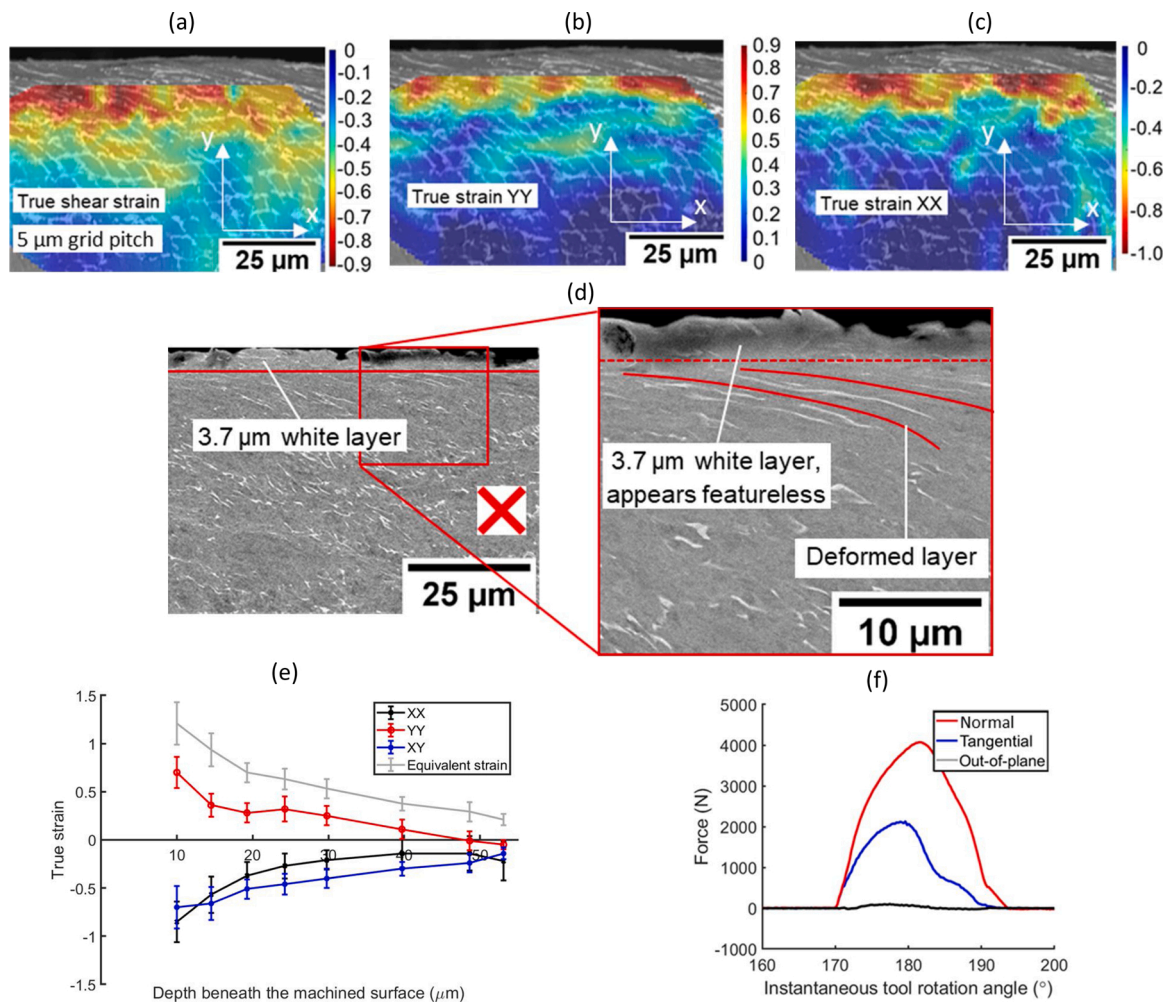


Fig. 8. (a-c) True strain maps, (d) an SEM image of the strain map region, (e) the true strain profiles with depth and (f) the corresponding forces during machining for a workpiece machined with a naturally worn insert (trial I). The grid pitch was 5 μm.

shear strain, the strain normal to the surface (ϵ_{yy} , Fig. 8(b) and (e)) shows a banded deformation field where layers of material are barely deformed in the Y direction at large depths, while heavily distorted grids can be observed in the adjacent layers near the surface. The large tensile strain in the y-direction occurred despite the 4 kN compressive normal force measured in this trial, as shown Fig. 8(f). This can also be attributed to tensile deformation in front of the cutting tool and is explored further in the discussion section.

3.2. The effect of cutting speed on machining-induced deformation

The strain developed in the workpiece near-surface at high (80 m/min) and low (20 m/min) cutting speeds when using worn inserts with the edge radius of 85 μm are shown in Fig. 9(a) and (b), respectively. Grids with 20 μm pitch were sufficient to capture the full strain profiles in identical locations on both samples where there was no significant grid damage. The lower cutting speed results in higher strain levels in the immediate subsurface, with a shear strain of about -0.8, compared with the measured value of -0.5 in the case of the higher cutting speed trial. The optical micrographs of identical regions of the cutting arc indicate that a white layer was only produced when machining at the lower speed, as shown in Fig. 9(c) and (d). The evolution of plastic strain in both samples shows an almost similar trend of all the measured strain components, with approximately a 20 μm greater depth of plastically deformed layer at the lower cutting speed, as shown in Fig. 9(e).

The increased magnitude and depth of plastic strain imparted in the

machined surface at the lower speed condition is supported by the increased contact length indicated by the larger angular range for normal and tangential cutting forces at the lower speed condition, as shown in Fig. 9(f). For both the applied cutting speeds, the normal force was maximum towards the end of tool engagement, as identified previously when using the worn inserts (Figs. 5(f) and 6 (f)), and this can be used to infer a large frictional contact between the tool flank face and the workpiece leading to dragging. The tangential forces, by contrast, were largest at the start of the cut, as would be expected during climb milling due to the maximum initial chip thickness. It should be noted that the larger cutting force measured at 20 m/min could be related to slightly larger achieved depth of cut of 0.28 mm (at maximum a/r of 0.72), compared with 0.25 mm (at a/r of 0.64) at 80 m/min.

Additionally, the increase deformation rate during machining with the higher cutting speed may have led to higher local flow stress at the cutting zones and hence smaller plastic deformation due to the increased resistance of the material against the imposed deformation. This can directly be linked to the higher local stresses at the applied strains, and consequently reaction forces, leading to more tool deflection, due to the increased material hardening, and reduced achievable depth of cut. Although high temperatures will be generated during chip formation due to the frictional and mechanical work (Liang et al., 2020), the effect of strain rate hardening seems to be dominant compared with the thermal softening at the higher cutting speed. Therefore, the strain rate hardening was the dominant mechanism compared to the thermal softening when using the higher cutting speed.

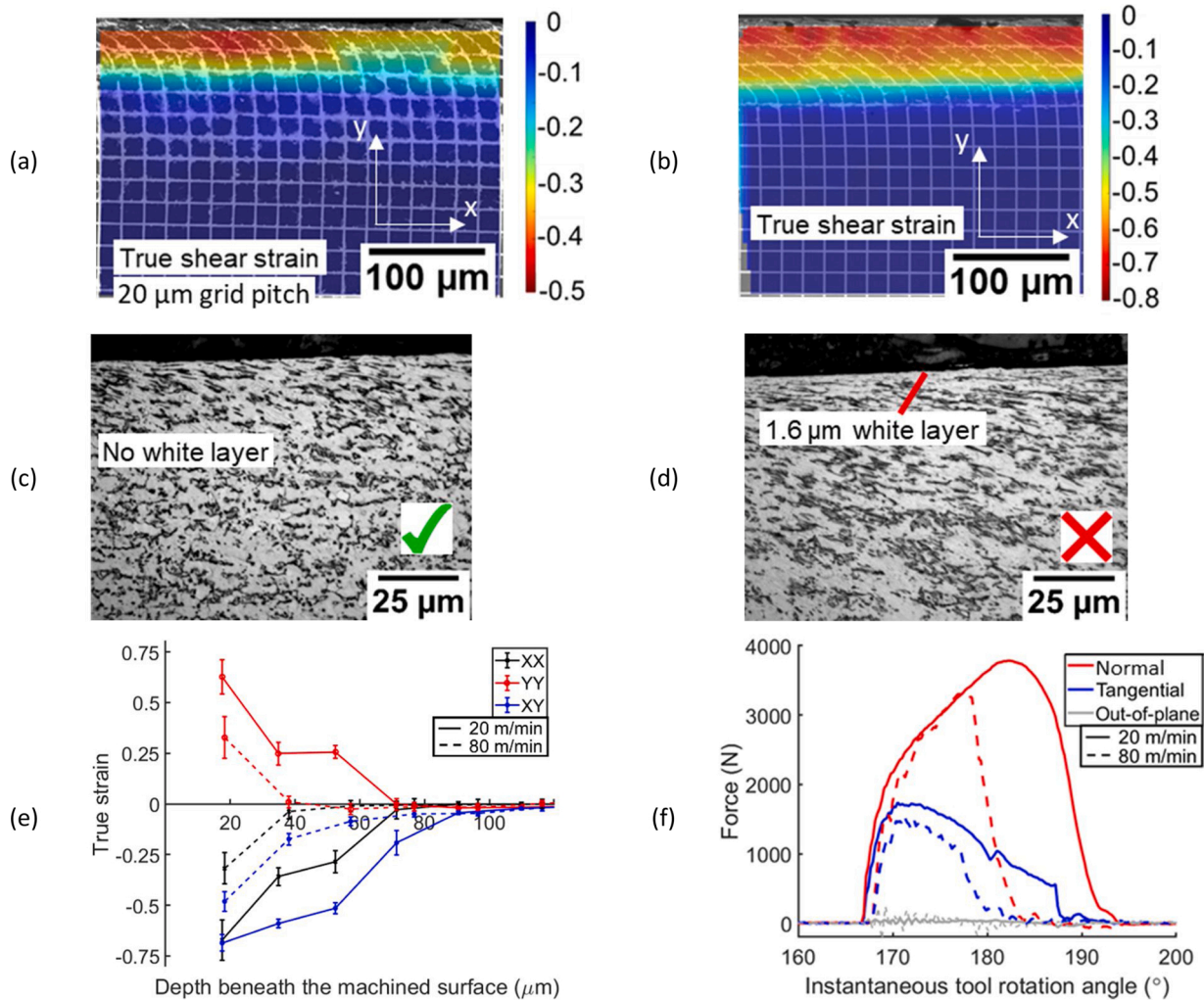


Fig. 9. True shear strain maps for a surface machined at (a) 80 m/min (trial V) and (b) 20 m/min (trial III) with the corresponding micrographs shown in (c) and (d), respectively. The measured strain profiles and machining forces are shown in (e) and (f). The grid pitch was 20 μm.

3.3. The effect of climb vs conventional milling on strain evolution in the machined surface

Fig. 10 (a) and (b) compares the measured near-surface strain distribution in the workpiece following climb and conventional milling, respectively, with the corresponding microstructures shown in Fig. 10 (c) and (d). Although larger ϵ_{xy} plastic strains were measured after climb milling, the overall depth of deformation, as shown in the ϵ_{xx} and ϵ_{yy} profiles in Fig. 10(e), is comparable for both operations. In both trials, the 0.5 mm desired depth of cut was not achieved, with only 0.25 mm (maximum a/r of 0.72) and 0.37 mm (a/r of 0.88) of material removed for the climb and the conventional milling, respectively. The reduced depth of cut for climb milling is responsible for the lower tangential force measured, as shown in Fig. 10(f). For both operations, the normal force reached a maximum of approximately 3.3 kN at the end of cut, due to failure to achieve the desired depth of cut which led to large compressive forces during rubbing when a/r was low. The comparable depths of deformation and strain in the cutting direction, ϵ_{xx} , despite the greater than 50 % increase in tangential force from climb to conventional milling, indicated that the tangential loading has minimal effect on the subsurface deformation. Therefore, the compressive normal force has a greater impact on the development of the deformed layer, as identified when reporting the results from the trials investigating cutting edge radius. Although no white layer was produced in the vicinity of these strain maps for climb or conventional milling, it was found when

inspecting the full machined surface that a white layer was only generated during the climb milling operation. However, due to damage of the grid in this region, it was not possible to compare strain measurements in this location on both samples.

4. Discussion

4.1. Plastic deformation and its role in the white layer formation

According to the measured local strains and microstructural analysis of the machined surfaces, SPD, rather than phase transformation is driving the white layer formation in the studied material under the applied machining conditions. This is aligned with previous investigations under comparable cutting conditions (Brown et al., 2019). Typically, high speeds and deformation rates have been associated with white layer formation, however, these white layers are often formed via phase transformation, and it is well-known that this mechanism is favourable at higher cutting speeds (Hosseini et al., 2015). By contrast, at lower speeds, the SPD mechanism is dominant and the formation of white layers at only the lower cutting speed used in this study proves that SPD rather than phase transformation was the active mechanism. It is reported (Telrandhe et al., 2017) that the depth of microstructural deformation in Ti-6Al-4V measured from microscopy analysis can be greater for lower cutting speeds so the formation of a plastic deformation-induced white layer at lower speeds is not unexpected.

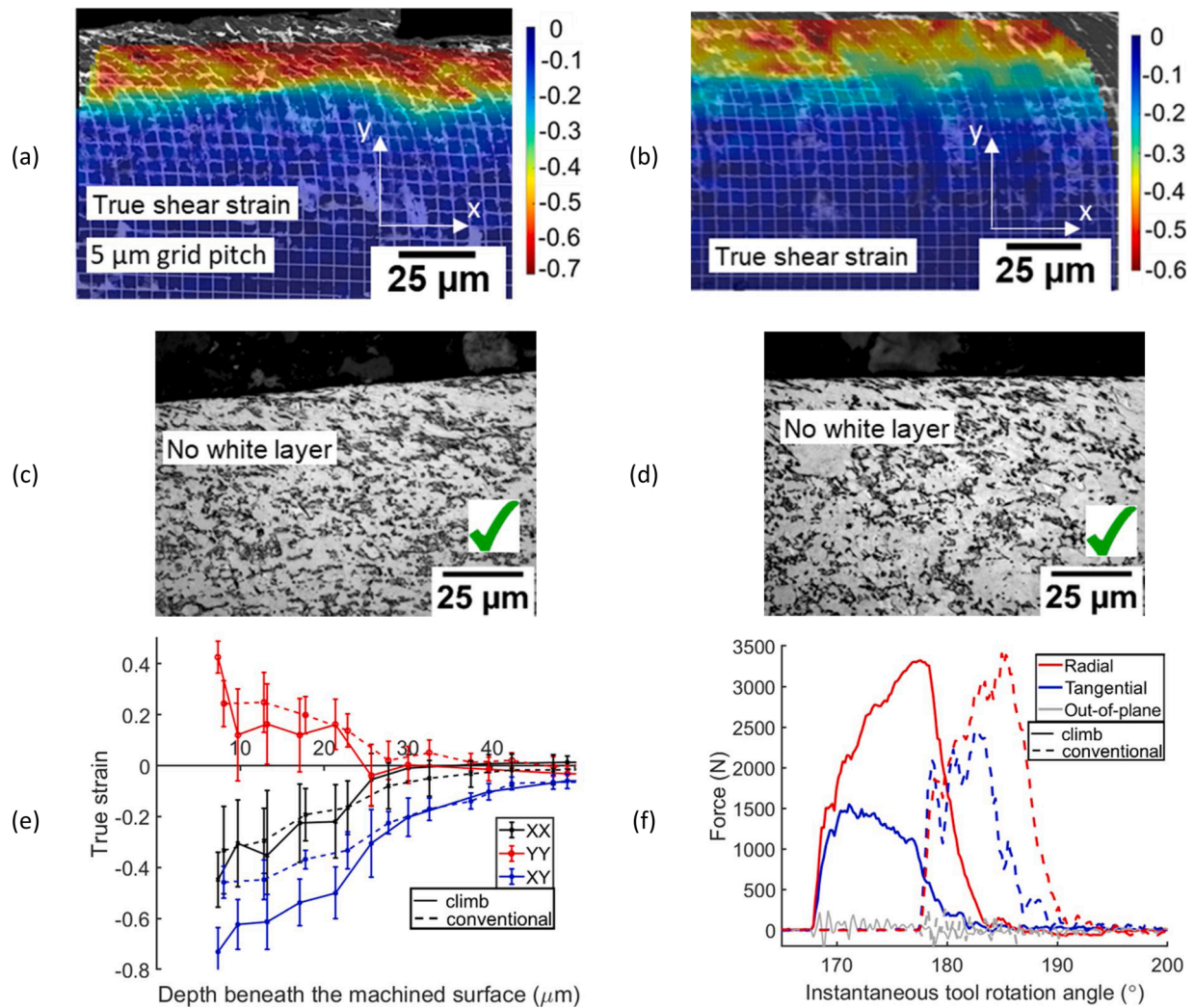


Fig. 10. True shear strain maps for a surface machined using (a) climb milling (trial V) and (b) conventional milling (trial VI) with corresponding micrographs in (c) and (d), respectively. The measured strain profiles and forces are shown in (e) and (f). The grid pitch was 5 μm.

The lower cutting speeds results in a smaller heat flux generation (Karaguzel and Budak, 2018) and the generated heat is pushed out of the deformation zone very quickly by the chip removal and the coolant effect, therefore the temperature and the induced thermal energy would not be sufficient to cause an $\alpha \rightarrow \beta$ phase transformation, therefore there is a higher tendency for SPD white layer formation at lower cutting speeds, as reported previously (Brown et al., 2019). The continuous dynamic recrystallization under the strain rates and temperatures generated during machining can lead to grain refinement (Brown et al., 2019) in titanium, due to its tendency for shear-localization. The plastic deformation with large strains near the surface provides the energy for recrystallization due to the increased dislocation density (Bacca et al., 2015), but the limited time at high temperature during machining restricts grain growth leading to the highly refined white layer microstructure which is not resolvable with optical microscopy. In contrast, for the swept grain region, the strain imparted into the material is not sufficient to initiate dynamic recrystallization and as such, the microstructure simply plastically deforms in the direction of the cutting speed, without grain refinement.

White layers were only formed when machining with worn inserts in the regions of the cutting arc where the cutting edge radius was larger than the theoretical instantaneous chip thickness and ploughing was the active deformation mechanism. Therefore, the ploughing and the induced additional compressive and shear strain contribute significantly

to the formation of white layer in milled Ti-6Al-4V. In addition, the measured normal forces during cutting provide further evidence for SPD white layer formation as it is already reported that white layer formation in milling was associated with high compressive forces (Brown et al., 2019). The effect of the a/r ratio and the cutting forces on deformation are discussed in the next section.

The lack of a phase transformation white layer is further supported by the absence of localised melting in the deformed gold grids post-machining, as shown in Fig. 10. If the beta transus temperature of the titanium workpiece had been exceeded during machining then the gold grids, which have a melting point of 1064 °C, just above the typical transus temperature range for titanium, could have been expected to melt. Regions where the grid material appeared to have spread out in the plane of the workpiece, were only found away from the machined surface and therefore away from the region of greatest heat generation, as shown in Fig. 10. As such this change in grid shape must be attributed to the smearing of the grids when the two workpieces are clamped in the orthogonal jig due to the 100 nm thickness of the grids perpendicular to the polished surfaces, rather than melting. It should be noted that due to the short interaction time between the tool and workpiece it is possible that the conduction of heat into the grids would not have been fast enough to cause melting, however, if phase transformation was the dominant mechanism, then white layers would have been expected at higher cutting speeds, rather than in the lower speed condition, as

observed in these trials (Fig. 11).

Although it was not possible to quantify the strain in the white layer itself, due to the comparatively thin white layer relative to the grid size, even for the smallest 5 μm grid, profiles of strain with depth suggest that the largest magnitude of the ϵ_{xy} , ϵ_{yy} and ϵ_{xx} strains within the white layer region produced by the observed mechanism must exceed a strain of 0.7 with the total plastic equivalent strain of 1.2. The increasing distortion of grains in the swept grain region nearer to the white layer, as shown in Figs. 5(e), 7 (e) and 8 (e), suggests that the strain increases up to the machined surface and could reach values as high as 1 at the machined surface. The rapid increase towards the surface can be attributed to shear-localization, similar to that seen in the chips of machined titanium alloys (Komanduri and Hou, 2002). In the context of these trials, the shear-localization occurs as the heat energy arising from plastic deformation in the near-surface of the workpiece leads to thermal softening of a thin band, due to the low thermal conductivity of titanium which prevents the heat from dissipating rapidly into the bulk material. This softer shear band consequently undergoes further plastic deformation, enhancing the strain in the region immediately at the machined surface, relative to greater depths. According to the observed micrographs, a true equivalent plastic strain of less than 1.2 could lead to the severely deformed microstructure through SPD without white layer formation. This results in the presence of only a swept grain region, which is a detrimental surface integrity feature, nonetheless, due to the reduction in fatigue life associated with thicker sub-surface deformation layers (Hardy et al., 2014).

It should be noted that the critical strain of 1.2 measured in this study represents the deformation at the final deformed state of the material at the machined surface irrespective of the applied deformation history and cannot be considered a universal threshold for white layer formation in all cases, due the strain rate sensitivity of titanium which has been reported by Luo et al. (2010). Deformation at different temperatures and strain rates is known to affect the deformation behaviour of titanium, particularly with respect to formation of adiabatic shear bands, which are equivalent to white layers (Zhang et al., 1997). As such a white layer or adiabatic shear generation in a low strain rate compression test could not be predicted based on the strain threshold identified here. However, most machining operations can be considered high strain rate and as such this threshold may be an appropriate approximation in the general case of conventional machining speeds. Additionally, the white layers generated in this study were formed through SPD rather than phase transformation and due to the thermal

dominance of the latter, the same strain threshold would not be expected to hold.

Whilst the generated white layers were too thin compared to even the smallest micro-grid, this method of strain characterisation was successful in quantifying general sub-surface deformation at the conventional machining conditions. Therefore, it is expected that the developed technique can be used to determine the local deformation field when a thick white layer is formed. In most cases, the gold grids adhered strongly to the surface and deformed with the titanium, rather than peeling away, ensuring the plane strain deformation condition. By printing the grids into the workpiece rather than carving them, as with the micro-milling or FIB etching methods, the EBL micro-grids cannot affect the deformation behaviour and so it should be the preferred method of micro-grid production, particularly for measuring deformation on such a small scale.

4.2. The effect of cutting and tooling conditions on imparted deformation

As identified in the previous section, white layers were only generated in regions where the uncut chip thickness was smaller than the cutting edge radius. It is therefore apparent that this ploughing regime greatly increasing the magnitude of severe plastic deformation, beyond that experienced for identical cutting parameters when the a/r ratio is larger, as can be seen from the comparison provided in Fig. 12(a) and (b). Across all trials, larger subsurface deformation was directly linked with lower a/r ratio as comparable results have previously been reported in turned Inconel-718 by Sharman et al. (2015). A larger cutting edge radius increases the contact area of the tool and the volume of workpiece material which experiences machining with a negative rake angle, encouraging ploughing of the surface (Lucca et al., 1993). As such, the increased depth and level of deformation with a larger edge radius is to be expected as a greater amount of the workpiece material is ploughed under the cutting tool, rather than forming part of the chip. It should be noted that the naturally worn tool produced a surface with a thicker white layer and larger deformation in the near-surface region, as shown in Fig. 8, despite a smaller wear land compared to the artificially ground inserts. Therefore, the effect of cutting edge radius was the most significant factor on the resultant strain distribution in the machined surface in these trials.

The strain maps of Fig. 13(a) and (b) shows the distribution of ϵ_{xy} corresponding to regions of the cutting arc with a large and small uncut chip thickness, respectively. The most severe surface drag occurs at the regions of the workpiece contact where rubbing and ploughing are dominant, in the case of Fig. 13(b), with a/r of less than 0.2. It should be noted that due to the different microgrid sizes used across the cutting arc, the scale for the two strain maps is different, however, despite the inability to resolve the strain in the first 10 μm beneath the surface for $a/r > 0.8$, Fig. 13(a), the strain is still not as high at a depth of 10 μm as it is for $a/r < 0.2$ in Fig. 13(b).

3D topography maps of the artificially and naturally worn inserts shown in Fig. 14(a) and (b) indicate that despite a larger wear land in the artificially worn insert, the cutting edge radius is smaller compared to the naturally worn insert. The naturally worn insert also has less uniform wear, with notch wear present alongside flank wear and edge rounding, by contrast the artificially worn insert contains only flank wear and edge rounding relative to an unworn insert.

As explained in the results section, the strain rate sensitivity of Ti-6Al-4V has a direct influence on the deformation imparted by the machining operation. It was shown in Fig. 9(a) and (b) that the depth and magnitude of plastic deformation was greater at 20 m/min than at 80 m/min. larger deformation at lower cutting speeds (Li et al., 2017) as well as at higher cutting speeds (Patil et al., 2016) are both reported in the literature. Therefore, localised deformation should be dependent on the applied cutting conditions and machining operations used considering the plastic flow properties of titanium. In the present study it is believed that strain rate hardening had a prevailing effect on material

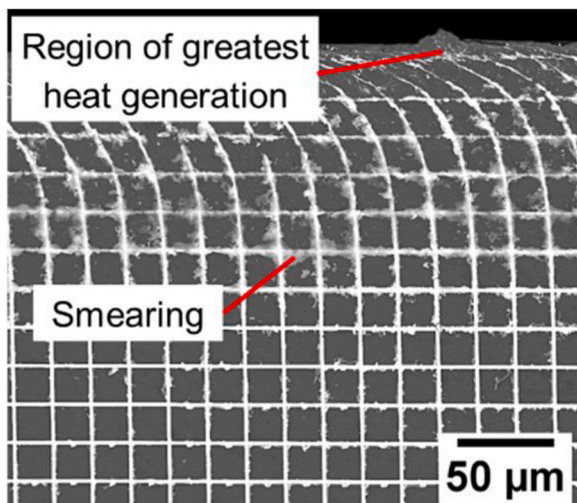


Fig. 11. A SEM micrograph of the deformed grids at the cutting surface using atomic contrast mode highlighting grids smearing about 50microns below the machined surface with no evidence of localized melting or smearing at the cut surface where the highest temperature is expected.

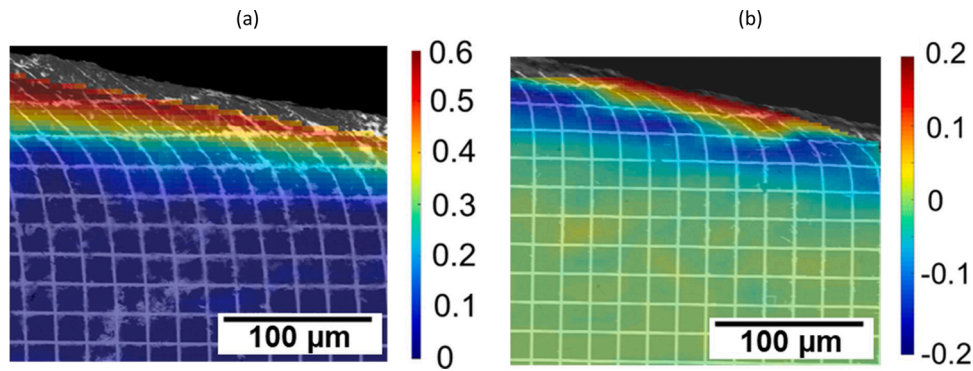


Fig. 12. True ϵ_{yy} maps from trial VI for (a) a cutting tool with a large edge radius relative to the uncut chip thickness and (b) a cutting edge radius smaller relative to the uncut chip thickness showing that the material is stretched in the y-direction (vertical in the micrographs) near the machined surface in the former, while a nonuniform deformation with tensile deformation at the surface directly followed by compression into the workpiece is formed in the latter case.

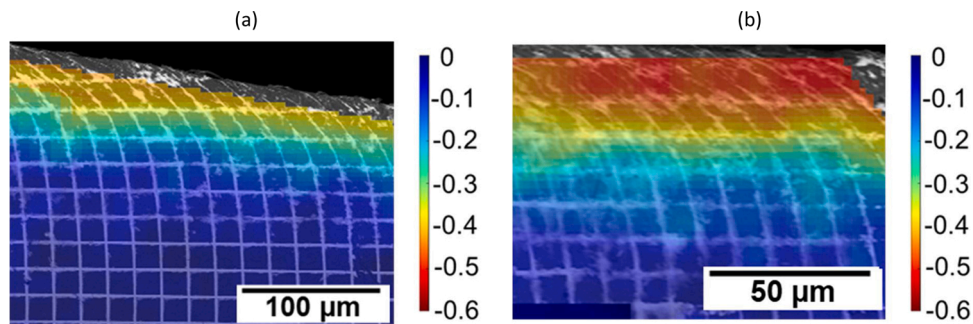


Fig. 13. True ϵ_{xy} maps from same trial VI in the different regions of the cutting arc corresponding to (a) a large uncut chip thickness ($a/r > 0.8$) and (b) a small uncut chip thickness relative to the insert cutting edge radius ($a/r < 0.2$).

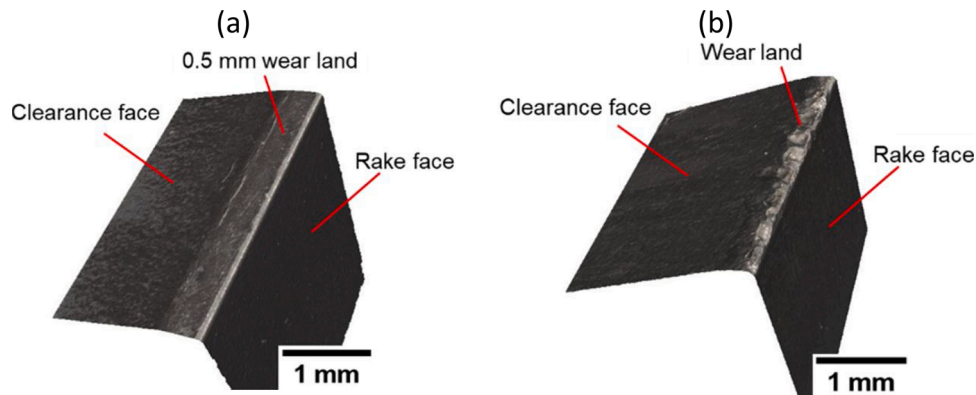


Fig. 14. A 3D topography map of (a) an artificially worn insert and (b) a naturally worn insert.

plastic deformation compared with the thermal softening at the higher cutting speed, thereby resulting in reduced deformation compared to the lower speed condition as the flow stress required for deformation was greater at the higher strain rate condition. This may have contributed to the slightly lower depth of cut achieved. The resulted lower strain rate in the case of using the lower cutting speed in addition to larger contact length are thought to have contributed to the larger deformation. As the tool was in contact with the workpiece for longer, there will have been increased heat generation in the machined surface which in these trials led to increased thermal softening relative to strain hardening.

With respect to the kinematics of the process, the larger plastic strains measured during climb milling (Fig. 10), would not normally be expected, as climb milling typically reduces the amount of ploughing that occurs before the uncut chip thickness is large enough for chip

formation. It is proposed that, in these trials, when forming a thick-to-thin chip during climb milling, the high initial chip thickness, where a/r was greater than 0.7–0.8, led to early deflection of the cutting tool, under high tangential and normal forces, such that for the majority of the cutting arc a smaller depth of cut was taken, resulting in an increased proportion of the cutting arc for which ploughing occurred, despite the 10 % larger edge radius for the insert used in the conventional milling cut. This error was most severe for the surfaces machined with naturally worn inserts, where the tool appeared to plough and rub the surface rather than remove the workpiece material as a chip and hence ploughing occurred for the whole cutting arc as the depth of cut achieved did not exceed the cutting edge radius. By contrast, for conventional milling, the initial chip thickness was small, so the initial deflection of the tool was lower, so a larger depth of cut was taken,

reducing the ploughing deformation compared to the climb milling case. In the conventional milling cut with the highest level of tool wear, the achieved depth of cut was still 4 times larger than the edge radius.

The positive value of the normal strain (ϵ_{yy} component) near the generated surface for the sample machined with a large cutting edge radius (Fig. 7(e)) means the material has extended, relative to its initial state, despite the compressive normal force on the surface, as shown in Fig. 7(f). This tensile deformation can be attributed to the deformation of the material in the primary deformation zone in front of the cutting tool, which causes positive ϵ_{yy} for material passing through the zone as illustrated in the strain map (Fig. 12(a)) from trial VI in the region of the cutting arc where chip formation was dominant. By contrast, the strain map of Fig. 12(b) for the same region from trial IV, in which the cutting edge radius was smaller, shows a tensile strain at the machined surface, due to the larger uncut chip thickness ratio for the smaller inserts, as previously reported in the literature (Ranganath et al., 2009), with a compressive layer beneath.

Plastic instability and shear localisation during chip formation in the workpiece material led to large levels of deformation in the vicinity of the tool tip. This deformation ahead of the tool and near the tool tip affects the plastic deformation measured in the machined surface as not all material that passes through the deformation zone in front of the tool goes on to form part of the chip, instead, some material subsequently passes underneath the cutting edge, as shown by Ghadbeigi et al. (2008) forming a region of material at the surface of the machined workpiece that has positive ϵ_{yy} , as illustrated in Fig. 15(a). Within the primary deformation zone, the deformation mode is mostly shear, however the material experiences some tensile deformation closer to the stagnation point before chip separation occurs. The material which does not form part of the chip then undergoes severe ploughing underneath the relief side of the tool leading to large additional shear deformation at the very surface.

The material machined with worn tools undergoes further deformation in the tertiary shear zone, after passing underneath the cutting edge, due to frictional contact between the tool flank face and the newly formed machined surface, as evidenced by the cutting force plots for worn inserts. Under this rubbing condition, the near-surface workpiece material is dragged in the direction of machining, resulting in increased shearing visible in the strain maps.

In the samples machined with new inserts and ground inserts with a small cutting edge radius, the change in the direction of ϵ_{yy} near the surface, from positive to negative with increasing depth, as shown in Fig. 7(e), can indicate that the deformation within the primary deformation zone is rather in mixed mode than pure shear where the material experiences tensile and shear deformation before chip separation occurs. The material at a greater depth beneath the workpiece surface does not

pass through the primary shear zone, instead, it is compressed when the material nearer the surface which does pass through the primary shear zone but does not form part of the chip, passes underneath the cutting edge, as shown in Fig. 15(b). This observation identifying the effect of the material passing underneath the cutting edge on the strain profile has been reported previously during orthogonal machining of aluminium alloys by Ghadbeigi et al. (2008).

The same compressed region is not observed for the trials using inserts with a larger cutting edge radius. This can be attributed to the increased size of the primary deformation zone which results in a greater volume of material near the surface that experiences shear deformation and still passes underneath the cutting edge. This depth of this region of material encompasses the region which experiences compression with a smaller cutting edge radius, hence this region is not present when the cutting edge is larger. The tensile strain near the surface is increased when using inserts with a larger edge radius due to the reduced depth of cut achieved, which results in ploughing of material towards the end of the cutting arc due to the small uncut chip thickness in relation to the edge radius.

5. Conclusions

The micro-grid method has been used to measure the strain distribution in orthogonally milled surfaces with different surface integrity states machined with a range of machining conditions. The measured strain maps, together with the observed microstructural morphologies of the machined surface, indicate that an individual true strain component greater than 0.7 (with an equivalent strain of 1.2) is required to initiate white layer formation through the SPD dominated mechanism in Ti-6Al-4V. Higher levels of sub-surface deformation and, therefore, the potential for white layer formation through SPD is promoted when machining with cutting tools with a larger cutting edge radius at lower cutting speeds. In these experiments, a white layer was found to form only in regions, during orthogonal milling, where the cutting edge radius was larger than the instantaneous chip thickness, particularly for the case of rubbing with zero chip thickness. This localised white layer formation was attributed to the greater proportion of material that is ploughed under the cutting tool for a larger cutting-edge radius, particularly when the instantaneous chip thickness is small. As such the edge-radius and consequently the ploughing effect was deemed to have a larger influence on the resultant strain distribution than the insert wear land, due to its impact on the size of the deformation zone in front of the tool.

Future studies should aim to quantify the plastic strain within a white layer which is thicker than the EBL micro-grid pitch, by machining a material such as IN-718 which is prone to thick white layer formation. The strain distribution associated with phase transformation white

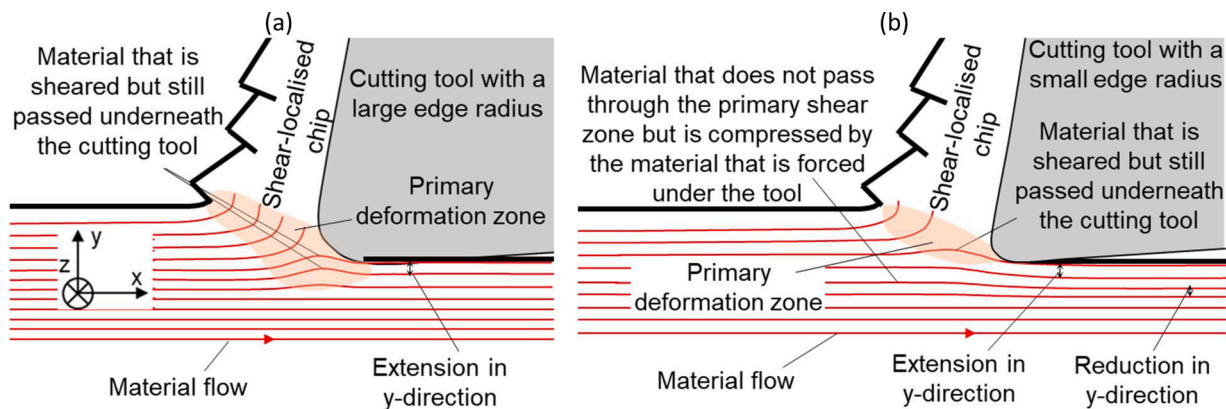


Fig. 15. Schematics showing (a) the extension of material in the y-direction near the machined surface for a cutting tool with a large edge radius relative to the uncut chip thickness and (b) the extension and reduction of material in the y-direction near the machined surface for the case where the cutting edge radius is smaller relative to the uncut chip thickness.

layers should also be compared to SPD white layers in hard turned steel, in which both types of white layer formation can occur.

CRedit authorship contribution statement

M. Brown: Conceptualisation, Investigation, Methodology, Software, Writing- original draft& editing, Formal analysis, Visualization. **R. M'Saoubi:** Supervision, Resources, Writing-review and editing, Funding acquisition. **P. Crawford:** Supervision, Resources, Writing-review and editing, Funding acquisition. **A. Mantle:** Supervision, Resources, Writing-review and editing, Funding acquisition. **J. McGourlay:** Supervision, Resources, Writing-review and editing, Funding acquisition. **H. Ghadbeigi:** Conceptualisation, Methodology, Supervision,

Resources, Formal analysis, Writing- original draft, review & editing, Funding acquisition.

Declaration of Competing Interest

The authors report no declarations of interest.

Acknowledgments

This research was supported by Rolls-Royce and Seco Tools in addition to the EPSRC [grant numbers EP/L016257/1, and EP/S013385/1]. Technical and scientific contribution of all the partners are greatly acknowledged.

Appendix A. Finite plastic deformation theory

Mathematically, deformation is the rate of change of shape with respect to position. The deformation gradient F (Eq. (A1)) describes the rotations and stretches required to transform between the initial and final conditions.

$$F_{ij} = \frac{\partial v_i}{\partial V_j} = \begin{bmatrix} \frac{\partial v_1}{\partial V_1} & \frac{\partial v_1}{\partial V_2} & \frac{\partial v_2}{\partial V_1} & \frac{\partial v_2}{\partial V_2} \end{bmatrix} \quad (\text{A1})$$

Where, v is a vector used to describe the deformed condition and V is a vector used to describe the undeformed condition. For the particular case of strain measurement from a micro-grid, as described by (Allais et al., 1994), the undeformed (V) and deformed (v) vectors take the form highlighted in Eq. (A2).

$$\begin{aligned} V_1 &= Ai + Bj, v_1 = ai + bj \\ V_2 &= Ci + Dj, v_2 = ci + dj \end{aligned} \quad (\text{A2})$$

The deformation gradient maps the undeformed configuration to the deformed configuration, as described mathematically in Eq. (A3).

$$v = F \cdot V \quad F = [abcd][ACBD]^{-1} \quad (\text{A3})$$

F can be decomposed into rotation R and stretch U components (Eq. (A4)).

$$F = R \cdot U \quad (\text{A4})$$

Polar decomposition is used to find, as the transpose of the rotation matrix is equivalent to the inverse, by definition. U is symmetric, therefore, the stretch tensor can be written as in Eq. (A5).

$$U = (F^T \cdot F)^{0.5} \quad (\text{A5})$$

To calculate the true strain, ϵ_T , U must be diagonalised by calculating principal strains using Eq. (A6).

$$\theta_p = \frac{1}{2} \left(\frac{2U_{12}}{U_{11} - U_{22}} \right) \quad (\text{A6})$$

The transformation matrix Q (Eq. (A7)) can then be used to diagonalise U through Eq. (A8) to arrive at the principal strain.

$$Q = [\cos(\theta_p) \sin(\theta_p) - \sin(\theta_p) \cos(\theta_p)] \quad (\text{A7})$$

$$U_{diag} = Q \cdot U \cdot Q^T \quad (\text{A8})$$

The diagonalised true strain matrix is calculated through Eq. (A9).

$$\epsilon_{T,diag} = \ln U_{diag} \quad (\text{A9})$$

True strain in the original coordinate system can then be found through a transformation using Q once more, as outlined in Eq. (A10)

$$\epsilon_T = Q \cdot \epsilon_{T,diag} \cdot Q^T = [\epsilon_{T,11} \epsilon_{T,12} \epsilon_{T,21} \epsilon_{T,22}] \quad (\text{A10})$$

References

- Allais, L., et al., 1994. Experimental characterization of the local strain field in a heterogeneous elastoplastic material. *Acta Metall. Mater.* 42 (11), 3865–3880.
 ASM-International, 1990. Properties of pure metals. Properties and Selection: Nonferrous Alloys and Special-Purpose Materials. ASM International.
 Bacca, M., Hayhurst, D.R., McMeeking, R.M., 2015. Continuous dynamic recrystallization during severe plastic deformation. *Mech. Mater.* 90, 148–156.

- Brown, M., et al., 2018. Destructive and non-destructive testing methods for characterization and detection of machining-induced white layer: a review paper. *CIRP J. Manuf. Sci. Technol.* 23, 39–53.
 Brown, M., et al., 2019. Quantitative characterization of machining-induced white layers in Ti–6Al–4V. *Mater. Sci. Eng. A* 764, 138220.
 Brown, M., et al., 2021. Non-destructive detection of machining-induced white layers through grain size and crystallographic texture-sensitive methods. *Mater. Des.* 200, p. 109472.
 Bushlya, V., et al., 2011. Characterization of white layer generated when turning aged inconel 718. *Procedia Eng.* 19, 60–66.

- Childs, T., 1971. A new visio-plasticity technique and a study of curly chip formation. *Int. J. Mech. Sci.* 13 (4), 373–387.
- Chou, Y.L., Evans, C.J., 1999. White layers and thermal modeling of hard turned surfaces. *Int. J. Mach. Tools Manuf.* 39, 1863–1881.
- Denkena, B., Grove, T., Maiss, O., 2015. Influence of the cutting edge radius on surface integrity in hard turning of roller bearing inner rings. *Prod. Eng.* 9 (3), 299–305.
- Edkins, K.D., Rensburg, N.J.v., Laubscher, R.F., 2014. Evaluating the subsurface microstructure of machined Ti-6Al-4V. *Procedia CIRP* 13, 270–275.
- Elmadagli, M., Alpas, A., 2003. Metallographic analysis of the deformation microstructure of copper subjected to orthogonal cutting. *Mater. Sci. Eng. A* 355 (1–2), 249–259.
- Fang-yuan, Z., et al., 2017. Influence of cutting condition on white layer induced by high speed machining of hardened steel. *Int. J. Adv. Manuf. Technol.* 77–84.
- Ghadbeigi, H., et al., 2008. Determination of micro-scale plastic strain caused by orthogonal cutting. *Int. J. Mach. Tools Manuf.* 48 (2), 228–235.
- Ghadbeigi, H., Pinna, C., Celotto, S., 2012. Quantitative strain analysis of the large deformation at the scale of microstructure: comparison between digital image correlation and microgrid techniques. *Exp. Mech.* 52 (9), 1483–1492.
- Griffiths, B.J., 1987. Mechanisms of white layer generation with reference to machining and deformation processes. *J. Tribol.* 109 (3), 525–530.
- Guo, Y.B., Warren, A.W., Hashimoto, F., 2010. The basic relationships between residual stress, white layer, and fatigue life of hard turned and ground surfaces in rolling contact. *CIRP J. Manuf. Sci. Technol.* 2 (2), 129–134.
- Hardy, M.C., et al., 2014. Characterising the integrity of machined surfaces in a powder nickel alloy used in aircraft engines. *Procedia CIRP* 13 (Supplement C), 411–416.
- Herbert, C., et al., 2014. Influence of surface anomalies following hole making operations on the fatigue performance for a nickel-based superalloy. *J. Manuf. Sci. Eng.* 136 (5), p. 051016 1-9.
- Hosseini, S.B., et al., 2015. Formation mechanisms of white layers induced by hard turning of AISI 52100 steel. *Acta Mater.* 89, 258–267.
- Karaguzel, U., Budak, E., 2018. Investigating effects of milling conditions on cutting temperatures through analytical and experimental methods. *J. Mater. Process. Technol.* 262, 532–540.
- Komanduri, R., Hou, Z.-B., 2002. On thermoplastic shear instability in the machining of a titanium alloy (Ti-6Al-4V). *Metall. Mater. Trans. A* 33 (9), 2995.
- Lee, E.H., 1969. Elastic-Plastic Deformation at Finite Strains.
- Li, A., et al., 2017. FEM-simulation of machining induced surface plastic deformation and microstructural texture evolution of Ti-6Al-4V alloy. *Int. J. Mech. Sci.* 123, 214–223.
- Liang, X., et al., 2020. Tool wear induced modifications of plastic flow and deformed material depth in new generated surfaces during turning Ti-6Al-4V. *J. Mater. Res. Technol.* 9 (5), 10782–10795.
- Lucca, D.A., Seo, Y., Komanduri, R., 1993. Effect of tool edge geometry on energy dissipation in ultraprecision machining. *CIRP Ann.* 42 (1), 83–86.
- Luo, J., et al., 2010. The variation of strain rate sensitivity exponent and strain hardening exponent in isothermal compression of Ti-6Al-4V alloy. *Mater. Des.* 31 (2), 741–748.
- Nie, G.-C., et al., 2020. Plastic strain threshold determination for white layer formation in hard turning of AISI 52100 steel using micro-grid technique and finite element simulations. *J. Manuf. Sci. Eng.* 142 (3).
- Patil, S., et al., 2016. The influence of cutting heat on the surface integrity during machining of titanium alloy Ti6Al4V. *Procedia Manuf.* 5, 857–869.
- Pottier, T., et al., 2014. Sub-millimeter measurement of finite strains at cutting tool tip vicinity. *Exp. Mech.* 54 (6), 1031–1042.
- Ranganath, S., Guo, C., Hegde, P., 2009. A finite element modeling approach to predicting white layer formation in nickel superalloys. *CIRP Ann.* 58 (1), 77–80.
- Sela, A., et al., 2020. Surface drag analysis after Ti-6Al-4V orthogonal cutting using grid distortion. *Procedia CIRP* 87, 372–377.
- Sharman, A., Hughes, J., Ridgway, K., 2015. The effect of tool nose radius on surface integrity and residual stresses when turning Inconel 718TM. *J. Mater. Process. Technol.* 216, 123–132.
- Telrandhe, S.V., Saxena, A.K., Mishra, S., 2017. Effect of microstructure and cutting speed on machining behavior of Ti6Al4V alloy. *J. Mech. Sci. Technol.* 31 (5), 2177–2184.
- Umbrello, D., 2013. Analysis of the white layers formed during machining of hardened AISI 52100 steel under dry and cryogenic cooling conditions. *Int. J. Adv. Manuf. Technol.* 64 (5), 633–642.
- Withers, P.J.B., Bhadeshia, H.K.D.H., 2001. Residual stress. Part 1 – measurement techniques. *Mater. Sci. Technol.* 17 (4), 355–365.
- Xu, X., et al., 2019. Grain refinement mechanism under high strain-rate deformation in machined surface during high speed machining Ti6Al4V. *Mater. Sci. Eng. A* 752, 167–179.
- Zhang, B., et al., 1997. Microstructures of surface white layer and internal white adiabatic shear band. *Wear* 211 (2), 164–168.
- Zhou, J.M., et al., 2011. Effects of tool wear on subsurface deformation of nickel-based superalloy. *Procedia Eng.* 19, 407–413.